Chemical Science

ROYAL SOCIETY OF CHEMISTRY

EDGE ARTICLE

View Article Online
View Journal | View Issue

Cite this: *Chem. Sci.*, 2025, **16**, 10372

All publication charges for this article have been paid for by the Royal Society of Chemistry

$Li_{3.6}In_7S_{11.8}Cl$: an air- and moisture-stable superionic conductor†

Ifeoluwa P. Oyekunle, [ac] Erica Truong, [ac] Tej P. Poudel, [bc] Yudan Chen, [ac] Yongkang Jin,[ac] Islamiyat A. Ojelade,[ac] Michael J. Deck, [ac] Bright Ogbolu, [ac] Md. Mahinur Islam, [ac] Pawan K. Ojha, [ac] J. S. Raaj Vellore Winfred, [a] Dewen Hou, [d] Hui Xiong, [e] Chen Huang [f] and Yan-Yan Hu *[abc]

All-solid-state batteries (ASSBs) have drawn significant attention as future energy storage technologies. Sulfide-based solid electrolytes are promising due to their high ionic conductivity and favorable mechanical properties. However, their reactivity with moisture, leading to decomposition and release of toxic gases such as H_2S, poses health and safety risks. In this study, a superionic conductor, $Li_{3.6}In_7S_{11.8}Cl$, which exhibits high structural stability in the presence of water and air, is synthesized. At 25 °C, $Li_{3.6}In_7S_{11.8}Cl$ delivers an ionic conductivity of 1.1 mS cm^{-1}, reaching 4.2 mS cm^{-1} post-exposure to humid air. Multimodal investigations reveal that trapped water inside the $Li_{3.6}In_7S_{11.8}Cl$ pellet facilitates ion conduction, which can be reversibly removed without compromising the structural integrity. The structure features a cubic-closed-packed anion sublattice with Li^+ ions diffusing *via* a three-dimensional isotropic network, confirmed by *ab initio* molecular dynamics simulations. ^6Li NMR and relaxometry identify the Wyckoff 16c and 8a as active Li^+ sites for ion conduction. The high ionic conductivity, long-term stable cycling performance, and moisture stability of $Li_{3.6}In_7S_{11.8}Cl$ make it a preferable electrolyte candidate for high-performance ASSBs.

Received 10th March 2025
Accepted 2nd May 2025

DOI: 10.1039/d5sc01907a

rsc.li/chemical-science

Introduction

Recent advancements in battery technology have led to the emergence of all-solid-state batteries, which address critical safety concerns associated with conventional Li-ion batteries.[1,2] Unlike their liquid-based counterparts, all-solid-state batteries eliminate the risk of electrolyte leakage and ignition attributed to flammable organic solvents.[1–5] Consequently, all-solid-state batteries are increasingly recognized as an advantageous alternative to traditional liquid-based systems.[3,5–8] Solid electrolytes (SEs) are indispensable for advancing all-solid-state batteries – engendering a need of favorable characteristics for solid electrolytes possessing. Ideally, a solid-state electrolyte should possess compatibility with electrodes, good mechanical properties, low electronic conductivity, good moisture stability, and high ionic conductivity.[9]

Sulfide solid electrolytes are favored due to their high ionic conductivity, rivaling conventional liquid electrolytes.[10,11] The lower electronegativity of sulfur, compared to oxygen, weakens the interaction with lithium ions and enhances their mobility within the lattice. Additionally, the larger ionic radius of sulfur creates wider migration pathways for lithium ions, further facilitating their transport.[12] Consequently, sulfide solid electrolytes exhibit improved ionic conductivities, rendering them highly promising for all-solid-state batteries.[13]

However, despite their high ionic conductivity, sulfide electrolytes suffer from poor air and moisture stability,[14] causing chemical decomposition and releasing toxic gases such as H_2S. Consequently, handling SSEs necessitates stringent safety measures, such as inert atmosphere for preparation and storage.[9,12,15–17] This limits their potential for wide-scale applications.[9] According to the hard and soft acids and bases (HSAB) theory, phosphorus (a hard acid) in thiophosphates prefers to react with oxygen (a hard base) compared to sulfur (a soft base).[17,18] This results in oxygen replacing sulfur during exposure to moisture, leading to rapid hydrolysis of the thiophosphate materials.[7,18] Consequently, effective strategies to evaluate and suppress this hydrolysis reaction are critical for the

[a]*Department of Chemistry and Biochemistry, Florida State University, Tallahassee, FL 32306, USA. E-mail: yhu@fsu.edu*

[b]*Materials Science and Engineering Program, Florida State University, Tallahassee, FL 32306, USA*

[c]*Center of Interdisciplinary Magnetic Resonance, National High Magnetic Field Laboratory, Tallahassee, FL 32310, USA*

[d]*Center for Nanoscale Materials Argonne National Laboratory, 9700 S Cass Ave, Lemont, IL 60439, USA*

[e]*Micron School of Materials Science and Engineering, Boise State University, Boise, ID, 83725, USA*

[f]*Department of Scientific Computing, Florida State University, Tallahassee, FL 32306, USA*

† Electronic supplementary information (ESI) available. See DOI: https://doi.org/10.1039/d5sc01907a

development of stable sulfide-based electrolytes for large-scale applications.[18]

In this study, we have synthesized a fast ion-conducting thioindate solid electrolyte, $Li_{3.6}In_7S_{11.8}Cl$, with conductivity reaching 1.1 mS cm^{-1} in the pristine state and 4.2 mS cm^{-1} when exposed to moisture. We employed a combined approach, utilizing solid-state NMR, synchrotron XRD, and electrochemical impedance spectroscopy (EIS), to characterize the Li^+ dynamics and elucidate the short- and long-range structures of $Li_{3.6}In_7S_{11.8}Cl$. Additionally, scanning electron microscopy (SEM) analysis with elemental mapping was performed, in conjunction with multinuclear NMR and XRD, to evaluate the structure integrity of $Li_{3.6}In_7S_{11.8}Cl$ upon exposure to humid air. $Li_{3.6}In_7S_{11.8}Cl$ demonstrates enhanced moisture stability, likely owing to the strong covalent interaction between In^{3+} and S^{2-}; this strong interaction effectively prevents oxygen from reacting with In^{3+} upon exposure to air or moisture, resulting in improved chemical stability of $Li_{3.6}In_7S_{11.8}Cl$. This work provides a robust strategy to improve the stability of sulfide superionic conductors in water and air.

Experimental

Material synthesis

LiCl (Sigma-Aldrich) and LiBr (Sigma-Aldrich) were dried under vacuum at 200 °C for 12 hours before synthesis. Li_2S (Alfa Aesar) and In_2S_3 (Sigma-Aldrich) were received and used without further purification. Stoichiometric amounts of Li_2S, In_2S_3, and LiCl were ground using an agate mortar and pestle in a Li : In : S : Cl mole ratio of 4 : 7 : 12 : 1 for 5 minutes. After grinding, the hand-milled powder was transferred into a ZrO_2 jar containing two 10-mm balls as a grinding aid. Mechanochemical mixing of the hand-milled powder in a ZrO_2 jar sealed under a vacuum was performed using a SPEX® 8000M MIXER/MILL high energy ball mill (SPEX®SamplePrep, USA) for 5 hours. Afterward, the ball-milled powder, typically 100–200 mg, was pressed into a 6-nm pellet under pressure of ~400 psi inside an argon-filled glovebox. The pellet was transferred into a quartz tube and sintered at 500 °C for 12 hours with a temperature ramping rate of 5 °C min^{-1}, followed by natural cooling under Argon. The resulting pellet had a thickness varying from ~1 mm to 2 mm, and the pellet appeared light yellow.

Structural characterization

Powder X-ray diffraction. The sintered pellet was finely grounded and packed in a zero-background sample holder. KAPTON® film (DUPONT™, USA) was used to seal the samples to prevent exposure to humid air. XRD was performed using a RIGAKU® D8 powder diffractometer with Bragg–Brentano geometry at a voltage of 45 kV and current of 40 mA with Cu-Ka radiation (a = 1.5406 Å). The data was collected within a 2θ range of 10–80° at a step size of 0.03° for 30 minutes.

Synchrotron X-ray diffraction. Synchrotron X-ray diffraction (XRD) was measured in capillary transmission mode at the 17-BM-B beamline, APS, Argonne National Lab, Illinois. The exact X-ray wavelength was refined to 0.24117 Å. The sample was loaded inside a special glass capillary, and the holder moved up and down during tests to ensure uniformity of measured results. Rietveld refinement of the XRD data was performed using GSAS-II.

Scanning electron microscopy. The morphology of the solid electrolytes was examined using a digital scanning electron microscope coupled with energy-dispersive X-ray spectroscopy. SEM/EDS studies were carried out using a JEOL JSM-IT800 SEM/EDX system with an accelerating voltage of 15.0 kV with a dwell time of 5 μs. The sintered pellets were mounted with carbon tape on an aluminum stub.

Solid-state NMR. ^{6}Li and ^{7}Li magic-angle-spinning (MAS) NMR experiments were performed using a Bruker Avance-III 500 spectrometer at Larmor frequencies of 73.6 MHz and 194.4 MHz, respectively. The MAS rate was 25 kHz. For ^{6}Li and ^{7}Li, single-pulse NMR experiments were performed using $\pi/2$ pulse lengths of 3.30 μs and 2.90 μs, respectively. The recycle delays were 500 s for ^{6}Li and 80 s for ^{7}Li. ^{6,7}Li NMR spectra were calibrated to $LiCl_{(s)}$ at −1.1 ppm. ^{7}Li T_1 relaxation time was measured with an inversion-recovery pulse sequence. Variable-temperature *in situ* ^{7}Li NMR experiments were performed using a Bruker Avance III 300 spectrometer at a Larmor frequency of 116.6 MHz from 298 to 343 K. ^{1}H MAS NMR experiments were performed using a Bruker Avance-III 500 spectrometer at a spinning rate of 25 kHz. Adamantane with a ^{1}H NMR peak at 1.83 ppm was used as the calibration standard.

Raman spectroscopy. Raman measurements were performed on the powder samples using a Horiba JY LabRam Evolution Raman Spectrograph with a 532-nm excitation laser and a grating size of 600 g mm^{-1}.

Thermogravimetric analysis. Differential scanning calorimetry (DSC) and thermogravimetric analysis (TGA) were performed on SDT Q600 (TA Instruments) at a heating rate of 5 °C min^{-1}. Argon, with a flow rate of 100 mL min^{-1}, was used as the purge gas.

Calculations

Density functional theory calculations. Density function theory (DFT) energy calculations and *Ab Initio* Molecular Dynamics (AIMD) simulations were conducted using the Vienna *ab initio* simulation package (VASP) and the projector augmented wave (PAW) approach.[19,20] Perdew–Burke–Ernzerhof generalized gradient approximation (GGA-PBE) was employed as the exchange–correlation functional.[21] The most recent pseudopotential files provided by VASP were used. For $Li_{3.6}In_7S_{11.8}Cl$, Python Materials Genomics (Pymatgen)[22] was employed to pre-screen the structures with different Li^+/vacancy, Li^+/In^{3+}, and S^{2-}/Cl^- orderings based on the experimentally refined crystal structure of $Li_{3.6}In_7S_{11.8}Cl$. A handful of $1 \times 1 \times 1$ supercells were generated. Electrostatic energy calculations for these generated supercells were carried out using Ewald summation techniques.[23] Geometry optimization was performed using DFT calculations. The AIMD simulation for $Li_{3.6}In_7S_{11.8}Cl$ was performed on the relaxed structure, using the canonical ensemble for 80 ps with a step time of 2 fs at a temperature of 900 K.

NMR calculations. Geometry relaxation and NMR chemical shielding computations were performed using plane-wave

density functional theory (DFT) *via* the Cambridge Serial Total Energy Package (CASTEP, v. 21.11),[24,25] which incorporates periodic boundary conditions within the pseudopotential approximation. The Perdew–Burke–Ernzerhof (PBE) exchange-correlation functional within the generalized-gradient approximation (GGA)[21] was utilized. A plane-wave basis set was truncated at a cutoff energy of 700 eV with a 4 × 3 × 4 *k*-point grid and on-the-fly-generated pseudopotentials. Atomic positions and lattice parameters were fully optimized using the Limited-memory Broyden–Fletcher–Goldfarb–Shanno (LBFGS) algorithm[26,27] until the forces were less than 0.1 eV $Å^{-1}$. For NMR chemical shielding calculations, a cutoff energy of 800 eV and a 4 × 3 × 4 *k*-point grid with on-the-fly-generated pseudopotentials were employed.

Bond valence site energy calculations. The softBV-v131 algorithm[28,29] was employed to compute the bond valence site energy (BVSE). Adjustments were made to the occupancies of mixed sites to address the challenges posed by mixed cation occupancy. Specifically, Li and In were removed from the 16d and 8a sites, respectively, to allow for Li occupancy at the 8a and In occupancy at the 16d site while accounting for stoichiometric ratios and charge neutrality. This approach allowed for accurately evaluating lithium diffusion pathways within structures demonstrating site disorder.

Electrochemical measurements

Electrochemical impedance spectroscopy (EIS). The sintered pellets were sandwiched between indium foils in a 6 mm cylindrical cell, and the potentiostatic EIS measurement was performed using a Gamry electrochemical analyzer. The ionic conductivity was determined using the resultant impedance from the equivalent circuit fitting of the Nyquist plots. Biologic SP-300 was utilized for variable-temperature EIS (VT-EIS) measurements in the CSZ microclimate chamber. The activation energy was calculated from the Arrhenius-type plots of the VT-EIS measurements. Electronic conductivity was measured using the DC polarization method.

Linear sweep voltammetry and galvanostatic cycling of ASSBs. Linear sweep voltammetry (LSV) and galvanostatic cycling were conducted on ASSBs. Carbon-composite half-cells were constructed using PEEK split cells to determine the electrochemical stability window. The composite cathode for galvanostatic cycling was prepared by drying TiS_2 (Sigma-Aldrich, 99.9%) at 200 °C for 12 hours, followed by ball milling to reduce particle size. $Li_{3.6}In_7S_{11.8}Cl$ was then combined with TiS_2 at a 1 : 2 mass ratio and ground. Li_6PS_5Cl, synthesized according to Patel *et al.*'s method[30] served as the separator. In assembling the half-cells, 12 mg of catholyte was spread onto one side of the Li_6PS_5Cl pellet to achieve an aerial loading of approximately 1.25 mA h cm^2, pressed at 300 MPa for 10 seconds, and then assembled with a Li–In alloy foil on the other side to form Li–In|Li_6PS_5Cl|2SE:TiS_2 (SE:$Li_{3.6}In_7S_{11.8}Cl$) half cells. The cells were sealed with vacuum grease and cycled under controlled conditions at 22 °C with a stack pressure of ∼30 MPa within the voltage window of 1–2.5 V *vs.* Li–In. For rate performance test, the cell was cycled 5 times at each of the following rates: 0.2C, 0.5C, 1C, and 2C, where *C* is the theoretical specific capacity of TiS_2, 239 mA h g^{-1}. These rates translate to current densities of 0.28 mA cm^{-2}, 0.70 mA cm^{-2}, 1.40 mA cm^{-2}, and 2.80 mA cm^{-2}, respectively. Subsequently, long-term stability testing was performed over 120 cycles at 0.2C.

Results and discussion

Structure

We utilized solid-state reactions to synthesize $Li_4In_7S_{12}Cl$ (see Experimental section for details). The phase purity was initially determined with X-ray powder diffraction, and the resulting pattern is shown in Fig. 1a. Notably, our pattern displays Bragg reflections that closely match that of $Li_4In_8S_{16}Sn_2$.[31] For precise determination of bulk structural parameters, including atomic coordinates, site occupancies, and thermal parameters of $Li_4In_7S_{12}Cl$, a high-resolution X-ray diffraction pattern was collected at the synchrotron beamline at APS (see Experimental section for details). All Bragg peaks were indexed to the $Fd\bar{3}m$ space group (Fig. 1b). Rietveld refinement was employed for structural and phase determination, and the refinement results are provided in Table S1.† Rietveld refinement revealed $Li_{3.6}In_7S_{11.8}Cl$ as the actual composition, with a trace $LiInS_2$ impurity. This was further validated by SEM-EDX analysis, which showed that the atomic ratio (In : S : Cl) closely matched the refined stoichiometry (Table S2†). This refined composition, $Li_{3.6}In_7S_{11.8}Cl$, will be used hereafter. Attempts have been made to synthesize $Li_{3.6}In_7S_{11.8}Cl$ with the stoichiometric ratios of the precursors but yielding a slightly unfavorable ionic conductivity (Fig. S1†) likely due to Li and S loss during the sintering steps.

$Li_{3.6}In_7S_{11.8}Cl$, like other spinels, features a face-centered cubic (fcc) arrangement of S^{2-}/Cl^- anions stabilized by interstitial cations. The anions form a cubic close-packed (ccp) lattice, while the cations are positioned in defined interstitial sites. The cations are located at 8a, 16c, and 16d sites, while anions occupy the 32e positions.[32,33] Specifically, the unit cell of $Li_{3.6}In_7S_{11.8}Cl$ consists of one tetrahedrally coordinated 8a and two octahedrally coordinated 16c and 16d lithium sites, denoted as Li_{8a}, Li_{16c}, and Li_{16d}, respectively. Sulfur and chlorine atoms co-occupy the 32e anionic site, yielding a disordered anion sublattice (Fig. 1c).

The structure exhibits two distinct planes (Fig. 1d): $(0\bar{1}1)$ and $(01\bar{1})$. The $(0\bar{1}1)$-plane features a 3D framework consisting of three edge-sharing 16c octahedra that face share with 8a tetrahedra. In addition, Li_{16c} octahedra face-shares with interstitial tetrahedral voids, which provide additional lithium transport pathways. The $(01\bar{1})$-plane contains edge-sharing Li_{16c} and Li_{16d} octahedra. With Li occupying 13.2% and In occupying 86.8% of the 16d octahedra, Li-ion transport within this layer becomes less favorable owing to channel blocking and lower anion polarizability that arises from the presence of higher amount of multivalent (M^{3+}) cation within its neighborhood.

Local structure and ion dynamics characterized using NMR

High-resolution ^6Li NMR spectroscopy was utilized to probe the local Li^+ environments in $Li_{3.6}In_7S_{11.8}Cl$, and four major resonances were observed (Fig. 2a). The resonance at 0.17 ppm is

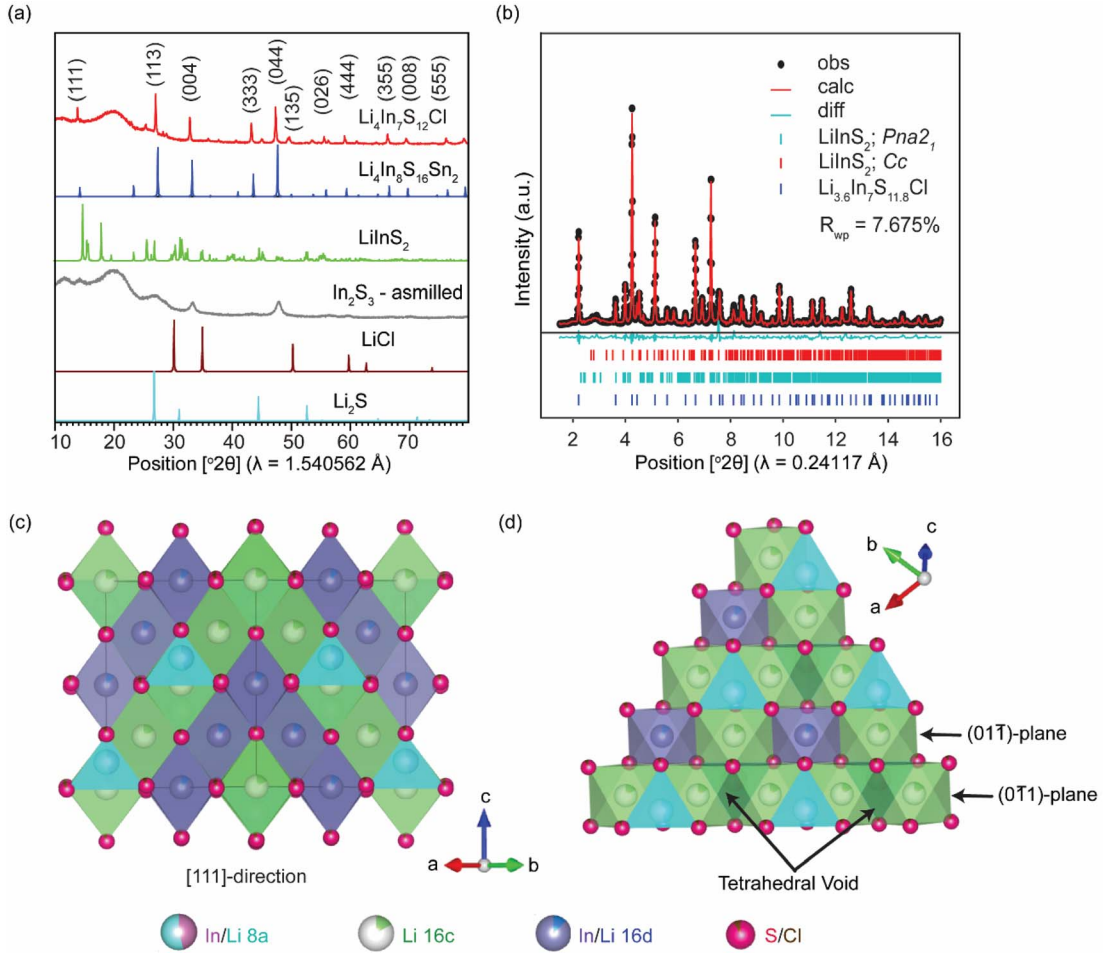

Fig. 1 (a) Powder X-ray diffraction patterns of the nominal $Li_4In_7S_{12}Cl$ and the precursors. ICSD patterns of $Li_4In_8S_{16}Sn_2$ and $LiInS_2$ are also shown as references. (b) High-resolution X-ray diffraction pattern and the corresponding Rietveld refinement of the nominal $Li_4In_7S_{12}Cl$, identifying the primary phase composition as $Li_{3.6}In_7S_{11.8}Cl$, which is used instead of $Li_4In_7S_{12}Cl$ hereafter. (c) and (d) The structure of $Li_{3.6}In_7S_{11.8}Cl$ with $Fd\bar{3}m$ space group obtained from the refinement of the high-resolution XRD pattern and viewed from different angles.

assigned to Li_{8a}. The resonances at 1.49 ppm and 2.03 ppm are assigned to Li_{16c} and Li_{16d}, respectively. These assignments correlate with the Li-occupancy determined from the diffraction results. The weak resonance at −0.84 ppm is attributed to a minor impurity phase, $LiInS_2$. This assignment was validated with DFT NMR calculations on $LiInS_2$, confirming a resonance

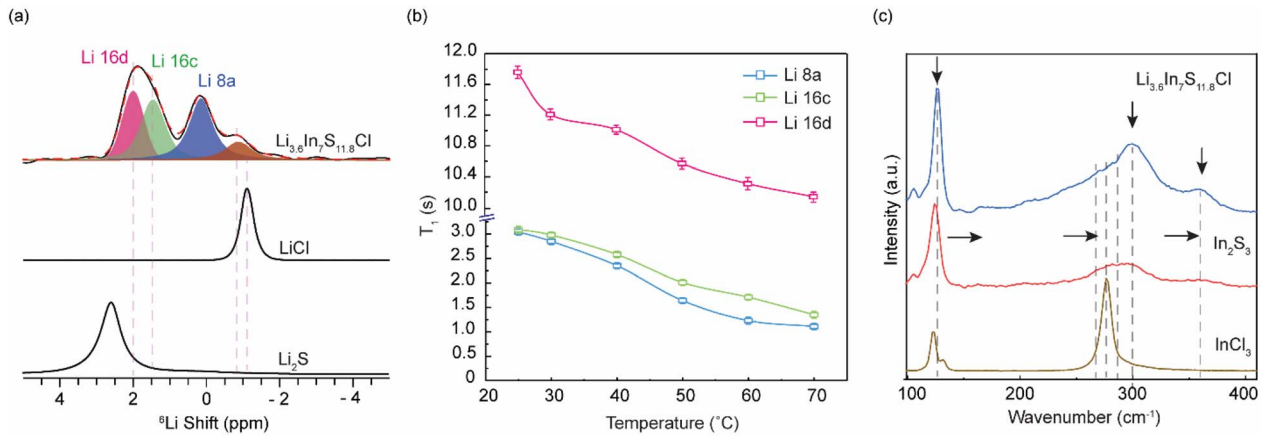

Fig. 2 (a) ^6Li NMR spectra with resonance assignment. ^6Li spectra of LiCl and Li_2S are shown as references. (b) ^7Li T_1 NMR relaxation times of $Li_{3.6}In_7S_{11.8}Cl$ as a function of temperature, revealing faster ion dynamics of Li_{8a} and Li_{16c}, compared with Li_{16d}. (c) Raman spectra of as-prepared $Li_{3.6}In_7S_{11.8}Cl$, In_2S_3, and $InCl_3$.

Table 1 ^{7}Li NMR relaxation times of different Li sites in the as-prepared (AP) and air/moisture-exposed (E) $Li_{3.6}In_7S_{11.8}Cl$

	^{7}Li, T_1 [s]		
Sample	Li_{8a}	Li_{16c}	Li_{16d}
$Li_{3.6}In_7S_{11.8}Cl$ (AP)	3.0	3.1	11.8
$Li_{3.6}In_7S_{11.8}Cl$ (E)	2.8	3.0	11.2

at −0.8 ppm (Table S3†). The quantification from ^{6}Li NMR area integrals is shown in Table S4.†

^{7}Li NMR relaxometry was utilized to study Li^+-ion mobility in $Li_{3.6}In_7S_{11.8}Cl$. As shown in Table 1 and Fig. 2b, the ^{7}Li T_1 relaxation time is significantly shorter for Li_{16c} (3.1 s) and Li_{8a} (3.0 s), compared to Li_{16d} (11.8 s). The Bloembergen–Purcell–Pound (BPP) model[34] provides a framework for understanding spin–lattice relaxation related to ion dynamics. The BPP model is described by $\frac{1}{T_1} = \frac{3\gamma^4\hbar^2}{10r_0^6}\left[\frac{\tau_c}{1+\omega_0^2\tau_c^2} + \frac{4\tau_c}{1+4\omega_0^2\tau_c^2}\right]$, where γ is the gyromagnetic ratio, $\hbar$ is the reduced Planck's constant, r_0 is the interatomic distance, $\omega_0 = \gamma B_0$ is the Larmor frequency, and B_0 is the external magnetic field strength. In the fast-motion regime ($\omega_o\tau_c \ll 1$), T_1 increases with increasing motional rate, while in the slow-motion regime ($\omega_o\tau_c \gg 1$), T_1 decreases with increasing motional rate. A motional rate can also lie in the intermediate region where $\omega_o\tau_c \approx 1$.

Variable-temperature ^{7}Li T_1 NMR relaxation time measurement reveals a decrease in T_1 relaxation time with increasing temperature and thus increasing motional rates for all the resonances, indicating that Li motion lies in the slow-motion regime ($\omega_o\tau_c \gg 1$).[34] Therefore, a shorter T_1 value will correlate with faster ion mobility. Consequently, Li_{8a} and Li_{16c} exhibit faster Li^+ ion motion as the relaxation time is significantly shorter than Li_{16d}. From ^{7}Li NMR line width analysis, the line width of Li_{8a} and Li_{16c} is narrower compared to Li_{16d} (Fig. S2†). A narrower line width may arise from Li^+ species with high mobility that averages out homogeneous and inhomogeneous line broadening.

Ion conduction properties determined with electrochemical impedance spectroscopy (EIS)

AC impedance spectroscopy was utilized to evaluate the ion transport properties of $Li_{3.6}In_7S_{11.8}Cl$. The Nyquist plot obtained at 25 °C is presented in Fig. 3a, and a representative Nyquist plot fitting of the data obtained at 0 °C using the equivalent circuit model is presented in Fig. 3b. The high-frequency semicircle with a capacitance of 0.6 pF corresponds to ion transport within the bulk of the solid electrolyte,[1,35,36]

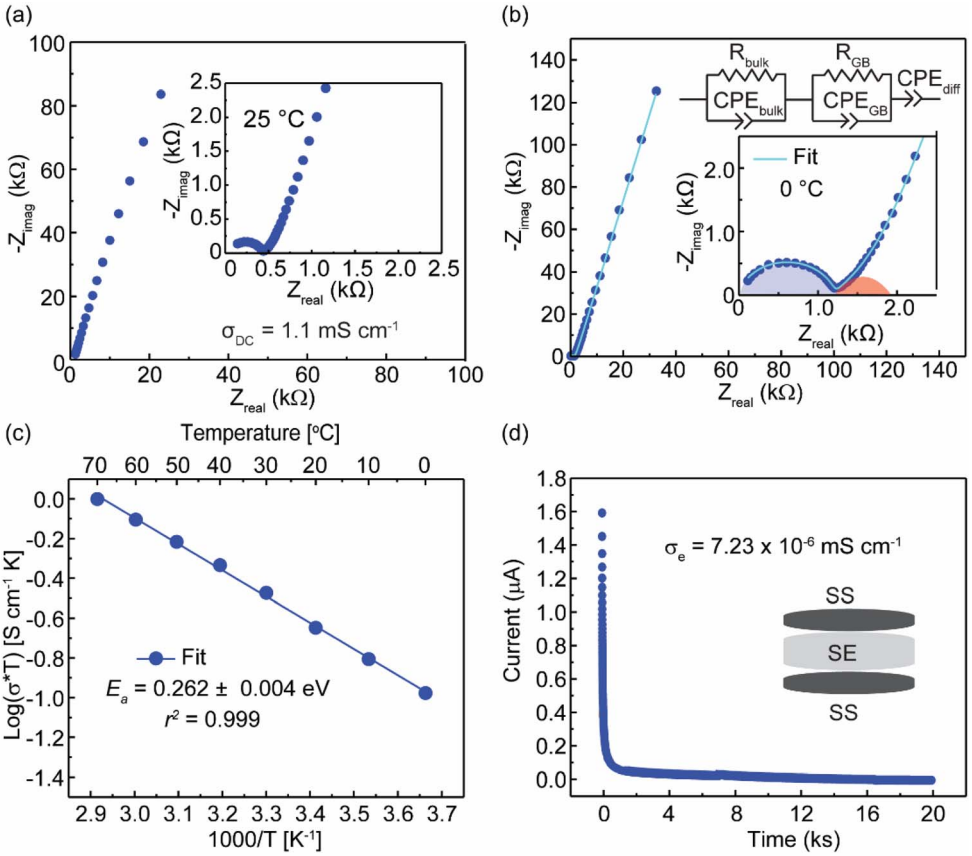

Fig. 3 (a) Nyquist plot at 25 °C for $Li_{3.6}In_7S_{11.8}Cl$. (b) Nyquist plot at 0 °C with equivalent circuit fitting (inset) for $Li_{3.6}In_7S_{11.8}Cl$. (c) Arrhenius plot and the extracted activation energy (E_a) for ion transport in $Li_{3.6}In_7S_{11.8}Cl$. (d) DC polarization curve of $Li_{3.6}In_7S_{11.8}Cl$ for the cell set up SS|SE|SS for determining the electronic conductivity of the SE, $Li_{3.6}In_7S_{11.8}Cl$.

while the medium-frequency semicircle with a capacitance of 1.2 nF represents the grain boundary contribution.[15] The ionic conductivity is calculated from the bulk impedance resistance using the formula $\sigma_{DC} = L/(R \times A)$. Here, L represents the pellet thickness, A denotes the surface area of the blocking electrode, and R is the resistance value obtained from the equivalent circuit fitting. An ionic conductivity of 1.1 mS cm^{-1} is obtained based on the resistance extracted from the fitting.

Variable-temperature EIS was carried out within the frequency range from 1 Hz to 7 MHz and the temperature range from 0 °C to 70 °C. Conductivities at various temperatures were calculated based on the Nyquist plots, and the Arrhenius-type plots were prepared to calculate the activation energy. Fig. 3c depicts the Arrhenius plots of $Li_{3.6}In_7S_{11.8}Cl$. An activation energy barrier (E_a) of 0.26 eV was determined from the linear fit of the Arrhenius plot. This value agrees with a site energy barrier of 0.26 eV obtained from the Bond Valence Site Energy (BVSE) calculation (Fig. S3†). The absence of any discontinuity throughout this temperature range, along with the observed linear Arrhenius behavior, indicates the thermal stability of $Li_{3.6}In_7S_{11.8}Cl$.[37] To verify that the conductivity arises from Li^+ transport, the electronic conductivity of $Li_{3.6}In_7S_{11.8}Cl$ was determined to be 7.23×10^{-6} mS cm^{-1} using the direct current (DC) polarization method at a constant voltage of 0.1 V (Fig. 3d). The relatively low electronic conductivity indicates negligible electronic contributions to the overall conductivity.

Lithium-ion transport *via* AIMD simulation

Ab initio molecular dynamics (AIMD) simulations are performed on the relaxed supercell (1 × 1 × 1) of $Li_{3.6}In_7S_{11.8}Cl$. Mean square displacements (MSD) and distribution probability of Li^+ at 900 K are extracted from the AIMD simulations (Fig. 4). The MSD of Li^+ illustrates the diffusion trajectories along the *a*, *b*, and *c* lattice directions (Fig. 4a). Notably, the MSD of Li^+ is similar along the *a*, *b*, and *c* directions, indicating a 3D diffusion for Li^+ in the $Li_{3.6}In_7S_{11.8}Cl$. Fig. 4b provides a 3D visualization of Li^+ density distribution within the relaxed $Li_{3.6}In_7S_{11.8}Cl$ crystal lattice (1 × 1 × 1), highlighting the primary lithium-ion sites labeled as Li_{8a}, Li_{16c}, and Li_{16d}. The yellow isosurfaces represent regions of high Li^+ probability density, indicating potential conduction pathways through the crystal lattice. This Li^+ density map reveals a complex, interconnected lithium diffusion network, further suggesting a 3D diffusion pathway for Li^+. These results underscore the high ionic conductivity of $Li_{3.6}In_7S_{11.8}Cl$, driven by the extensive 3D diffusion network.

Moisture stability of $Li_{3.6}In_7S_{11.8}Cl$

A significant challenge for large-scale production of sulfide solid electrolytes is their poor stability against atmospheric moisture. Even low levels of moisture in the environment have been reported to trigger spontaneous hydrolysis reactions, causing material degradation, compromised performance, and the release of toxic H_2S gas.[38,39] Broadly, on exposure of solid electrolytes to moisture, decomposition products such as LiCl,[40–42] Li_2S,[40,42,43] LiOH,[41–43] $LiOH \cdot H_2O$,[39,42] and In_2O_3 (ref. 41) may be formed. These decomposition compounds exhibit poor ionic conductivity and significantly increase interfacial impedance when formed on the surface of sulfide SSE particles.[41,43] $Li_{3.6}In_7S_{11.8}Cl$ was exposed to air for 2 hours (relative humidity of 52%) to assess the impact of moisture on its average structure, short-range structure, morphology, and ionic conductivity. Fig. 5c displays the XRD patterns of $Li_{3.6}In_7S_{11.8}Cl$ before and after 2 hours of exposure to humid air at room temperature. A comparison of the diffraction pattern of as-prepared and moisture-exposed samples reveals insignificant modification of the average structure. Particularly, no new peaks were formed post-exposure. This is consistent with ^{6}Li NMR results of the moisture-exposed sample (Fig. 5d) – confirming the absence of LiCl, LiOH, or Li_2S, post-exposure.

The Hard–Soft Acid–Base (HSAB) theory predicts favorable interactions between soft acids (*e.g.*, Ge^{4+}, Sn^{4+}, In^{3+}) and soft bases (*e.g.*, S^{2-}).[38,44–47] These interactions lead to the formation of strong covalent bonds, potentially creating a stable framework with open channels.[44] To be specific, In^{3+}, classified as a soft acid, will preferentially interact with the soft base, S^{2-}.[47] This preferential bonding with sulfur prevents the hard base oxygen from reacting with In^{3+} upon exposure to moisture. As a result, $Li_{3.6}In_7S_{11.8}Cl$ exhibits improved moisture stability. A

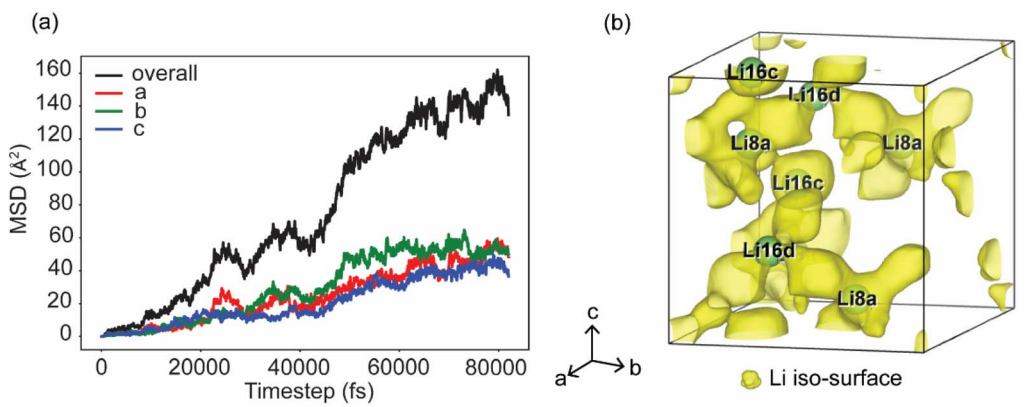

Fig. 4 (a) Mean square displacements of Li^+ in $Li_{3.6}In_7S_{11.8}Cl$ generated from AIMD simulations at 900 K. (b) Li^+ (yellow) probability density distribution in $Li_{3.6}In_7S_{11.8}Cl$ in a 1 × 1 × 1 supercell based on the AIMD simulations at 900 K.

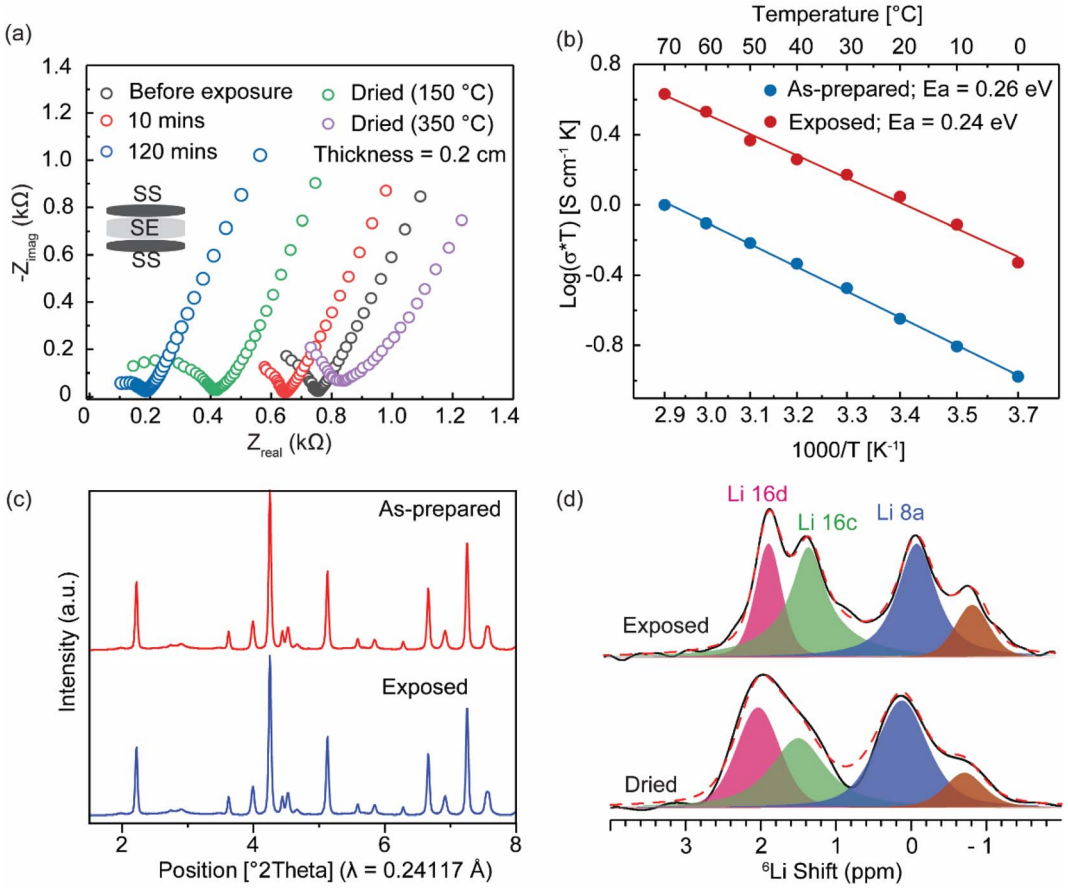

Fig. 5 (a) Nyquist plot for the as-prepared, humid-air-exposed, and dried $Li_{3.6}In_7S_{11.8}Cl$. (b) Arrhenius plot and the extracted activation energy (E_a) for ion transport in as-prepared and humid-air-exposed $Li_{3.6}In_7S_{11.8}Cl$. (c) SXRD patterns for as-prepared and air/moisture-exposed $Li_{3.6}In_7S_{11.8}Cl$. (d) ^6Li MAS NMR spectra of humid-air-exposed and dried $Li_{3.6}In_7S_{11.8}Cl$.

decrease in the activation energy (Fig. 5b) is observed for the moisture-exposed pellet (0.24 eV) relative to the as-prepared pellet (0.26 eV). Fig. 5a reveals a significant increase in ionic conductivity to 4.2 mS cm^{-1} on exposure to moisture – an observation in contrast to what has been reported for most sulfide solid electrolytes,[48–50] except layered structures where H_2O intercalates between the sheets.[51] However, the slightly increased electronic conductivity post-exposure (4.55×10^{-5} mS cm^{-1}, Fig. S4†) may suggest modifications of the local electronic environment and an increase in electron transport.

Raman spectroscopy, a valuable tool for elucidating the local structures of materials,[52,53] was employed to investigate the bonding between In^{3+} and S^{2-}. Fig. 2c presents the Raman spectra of the as-prepared $Li_{3.6}In_7S_{11.8}Cl$ and reference samples including In_2S_3 and $InCl_3$. According to the XRD pattern (Fig. 1a), In_2S_3 and $Li_{3.6}In_7S_{11.8}Cl$ primarily exhibits a disordered cubic spinel-type, α-In_2S_3 structure, confirmed by the absence of low-intensity peaks prominent in the tetragonal β-In_2S_3 structure.[54,55] Notably, the presence of Raman active modes at 125 cm^{-1} (E_g), 270, 291, 299 cm^{-1} (T_{2g}) and 357 cm^{-1} (A_{ig}) in In_2S_3 Raman spectrum (Fig. 2c) confirms that it belongs to the α-In_2S_3 structure type.[56,57] The Raman spectrum of $Li_{3.6}In_7S_{11.8}Cl$ exhibits a significant shift (blue shift) of the Raman peaks associated with In–S bonds to higher wavenumbers compared with In_2S_3, specifically to 127, 278, 300, 308 and 360 cm^{-1}.[53,58] This shift to higher wavenumbers signifies an increase in the vibrational energy of these bonds, indicating stronger In–S interactions.[59] Moreso, compared to the Raman spectrum of In_2S_3, the peak intensity is significantly higher for $Li_{3.6}In_7S_{11.8}Cl$. More intense peaks suggest increased Raman scattering efficiency, often a result of strong covalent bonding with more polarizable bonds. Therefore, both the blue shift and peak intensity increase support enhanced In–S covalent bonding in $Li_{3.6}In_7S_{11.8}Cl$.

Water uptake can influence cation mobility through solvation or altering the crystallographic structure.[60] Although hydration studies on solid Li^+ and Na^+ conductors are limited, existing research suggests enhanced Li^+ and Na^+ diffusion with water adsorption.[60] The adsorbed water may exist in different forms; for instance, free water clusters and loosely and strongly bound water have been identified in Nafion.[61,62] To understand the origin of the improved ionic conductivity of $Li_{3.6}In_7S_{11.8}Cl$ post-exposure, we performed ^1H and $^{6,7}Li$ NMR on the as-prepared and moisture-exposed-samples. For the moisture-exposed-sample, a peak at 4.7 ppm was observed in the ^1H NMR spectrum; in contrast, only the background resonance

(empty rotor) was observed for the as-prepared sample (Fig. S5†). The resonance at *ca.* 4.7 ppm in moisture-exposed $Li_{3.6}In_7S_{11.8}Cl$ indicates that the adsorbed water is more distinctly characterized as a bulk liquid rather than surface-bound. Increased Li^+ ion mobility in the moisture-exposed $Li_{3.6}In_7S_{11.8}Cl$ is indicated by faster ^7Li NMR T_1 relaxation (Fig. S6†) with decreased ^7Li NMR T_1 relaxation time (Table 1), and narrower peak width (Table S5†). Increased ionic conductivity in the moisture-exposed $Li_{3.6}In_7S_{11.8}Cl$ is therefore attributed to ion transport facilitated by the adsorbed water.

The SEM images and the EDS elemental mapping of In, S, Cl, and O for the as-prepared $Li_{3.6}In_7S_{11.8}Cl$ and moisture-exposed pellet are shown in Fig. 6a and b. Prior to ambient exposure, the as-prepared pellet demonstrates a highly compact structure. The initial SEM image reveals an uneven surface with loose particles; however, it is devoid of major cracks. Notably, the microstructure of the moisture-exposed sample does not change significantly. However, the pellet surface is smoother. Elemental mapping of the as-prepared $Li_{3.6}In_7S_{11.8}Cl$ reveals a uniform distribution of In, S, Cl, and a negligible amount of O. The negligible amount of oxygen likely results from the few seconds exposure to humid air during sample transfer into the SEM instrument. Similarly, In, S, Cl are uniformly distributed in the exposed pellet. In addition, a significant oxygen concentration is observed around the particles, likely from the adsorbed water. It is evident that the absorbed water does not disturb the $Li_{3.6}In_7S_{11.8}Cl$ structure but rather distributes on the surfaces of the particles. The enhanced microstructural stability of $Li_{3.6}In_7S_{11.8}Cl$ may be attributed to the structural stabilization from the strong covalent interaction of In^{3+} with S^{2-}, effectively preventing hydrolysis reactions.[18]

The hydrolysis resistance of $Li_{3.6}In_7S_{11.8}Cl$ was evaluated by full immersion of the solid electrolyte in deionized water (Fig. S7†). Throughout the exposure test, no significant changes were visually observed, indicating that its structure was not severely altered.[45] Further quantitative evaluation of hydrolytic resistance was performed by comparing the mass of the electrolytes before and after immersion. The mass remains almost constant at 140 mg – only reaching 139.4 mg after 1 hour, suggesting excellent hydrolysis resistance of $Li_{3.6}In_7S_{11.8}Cl$. TGA and DSC curves of the moisture-exposed sample are shown in Fig. S8.† To simulate non-oxidative environments, thermogravimetric analysis (TGA) and differential scanning calorimetry (DSC) were performed under an inert atmosphere at a constant heating rate from 0 °C to 700 °C. The initial thermal event, observed between 49 °C and 83 °C, reflects dominant endothermic peaks. This corresponds to removing physiosorbed water molecules, resulting in a mass loss of 3.37%. A minor endothermic event observed at *ca.* 350 °C is attributed to removing bulk water buried inside $Li_{3.6}In_7S_{11.8}Cl$.[63] Overall, the mass loss of 3.61% is due to water removal, indicating good thermal stability of $Li_{3.6}In_7S_{11.8}Cl$.

The exposed pellets were dried to investigate the impact of water removal on ion transport and structure. The impedance

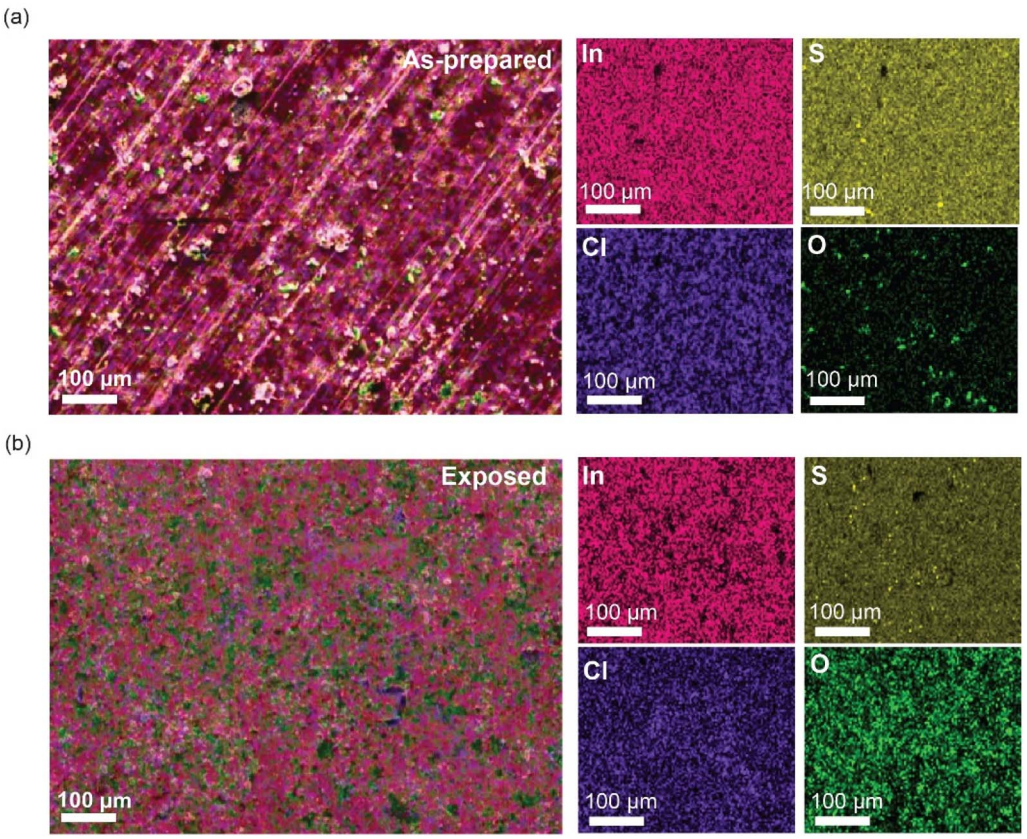

Fig. 6 SEM images and EDS elemental mapping of In, S, Cl, and O for (a) as-prepared and (b) moisture-exposed $Li_{3.6}In_7S_{11.8}Cl$.

plot reveals a decrease in ionic conductivity (4.2 mS cm^{-1} *vs.* 2.06 mS cm^{-1}) of the pellet dried at 150 °C for 12 hours relative to the moisture-exposed pellet. The SEM images and the EDS elemental mapping of the surface and cross-section of the dried pellet are shown in Fig. 7a and b. Elemental mapping reveals a minimal amount of oxygen on the surface of the dried pellet – indicating loss of surface water upon drying at 150 °C. The negligible amount of oxygen may stem from water re-adsorption during sample transfer into the instrument. However, ^{1}H NMR reveals only a slight decrease in the intensity of the bulk water resonance – suggesting that bulk water is retained (Fig. S5†) after extended heating at 150 °C for 12 hours. To confirm this observation, SEM and EDS data were collected on the cross-section of the pellet (Fig. 7b). A high amount of oxygen, evident within the cross-section, validates the presence of bulk water inside the pellet. The presence of bulk water correlates with higher ionic conductivity (Fig. 5a) of the pellet dried at 150 °C compared to the as-prepared pellet (2.06 mS cm^{-1} *vs.* 1.1 mS cm^{-1})

TGA experiment suggests a thermal event at *ca.* 350 °C; therefore, to further examine the effect of bulk water loss on the structural stability and ionic conductivity of the moisture-exposed solid electrolyte, the pellet was dried at 350 °C. The corresponding impedance plot is shown in Fig. 5a. A significant decrease in conductivity was observed (2.06 mS cm^{-1} *vs.* 0.98 mS cm^{-1}) relative to the pellet dried at 150 °C. However, the ionic conductivity does not deviate largely from that of the as-prepared pellet (1.1 mS cm^{-1} *vs.* 0.98 mS cm^{-1}), suggesting that water can be reversibly removed without compromising the structure or ion transport properties of the solid electrolyte. ^{1}H NMR confirms (Fig. S5†) the complete removal of bulk water after drying at 350 °C, further validated by significantly reduced oxygen distribution from cross-section elemental mapping of the dried pellet (Fig. S9†).

Proposed mechanism of ion transport in moisture-exposed $Li_{3.6}In_7S_{11.8}Cl$

Enhanced ionic conductivity of moisture-exposed polycrystalline solid electrolytes has been linked to the presence of adsorbed water at grain boundaries.[64] On exposing $Li_{3.6}In_7S_{11.8}Cl$ to moisture, the scanning electron microscopy (SEM) images of $Li_{3.6}In_7S_{11.8}Cl$ revealed the distribution of adsorbed water on the surface of- and around the grains (Fig. 7b). ^{6}Li NMR analysis (Fig. 5d) suggests that Li^+ in $Li_{3.6}In_7S_{11.8}Cl$ is not hydrolyzed or transformed into other chemical phases in the presence of the absorbed water.[60] The adsorbed water may effectively soften or plasticize the grain boundaries without compromising its integrity, facilitating Li^+ hopping between grains and reducing the energy barrier for Li-ion migration. To assess the impact of the adsorbed-water around grain boundaries on Li^+ transport, we performed EIS analysis to separate the resistive contributions from the bulk and grain boundaries. By fitting the impedance spectra to equivalent circuit models, the grain boundary resistance and bulk resistance can be independently extracted. Our EIS analysis (Fig. 8 and Table S6†)

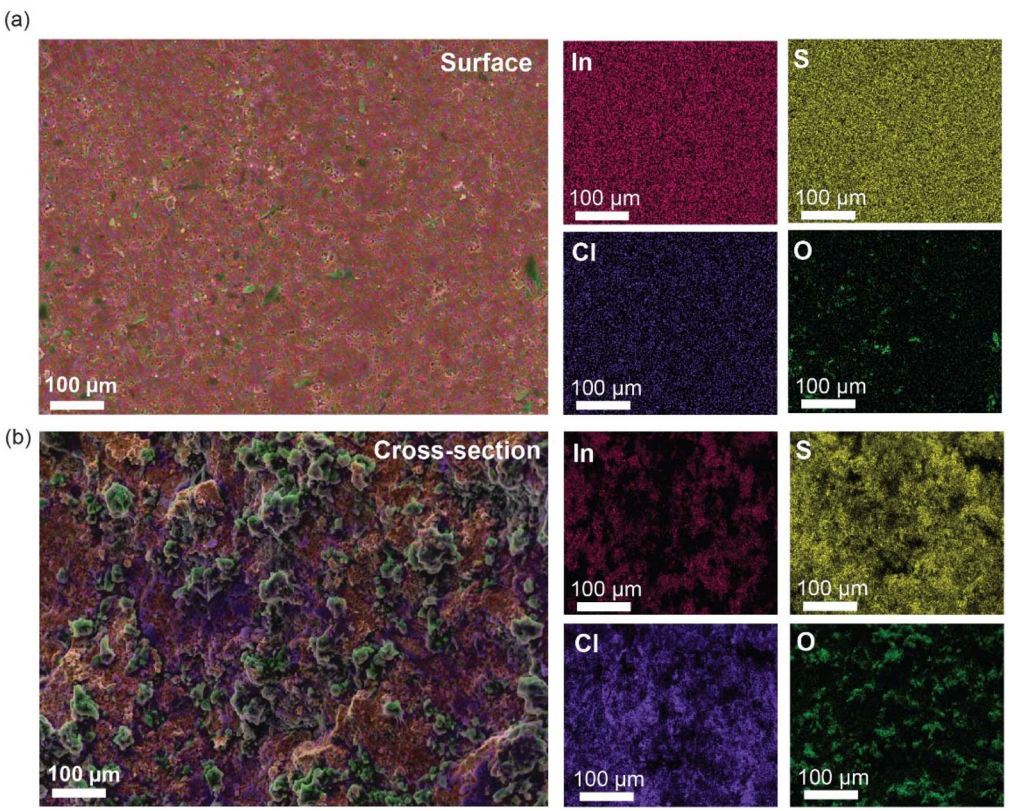

Fig. 7 SEM image and EDS elemental mapping of In, S, Cl, and O for the (a) surface (b) cross-section of $Li_{3.6}In_7S_{11.8}Cl$ pellet dried at 150 °C.

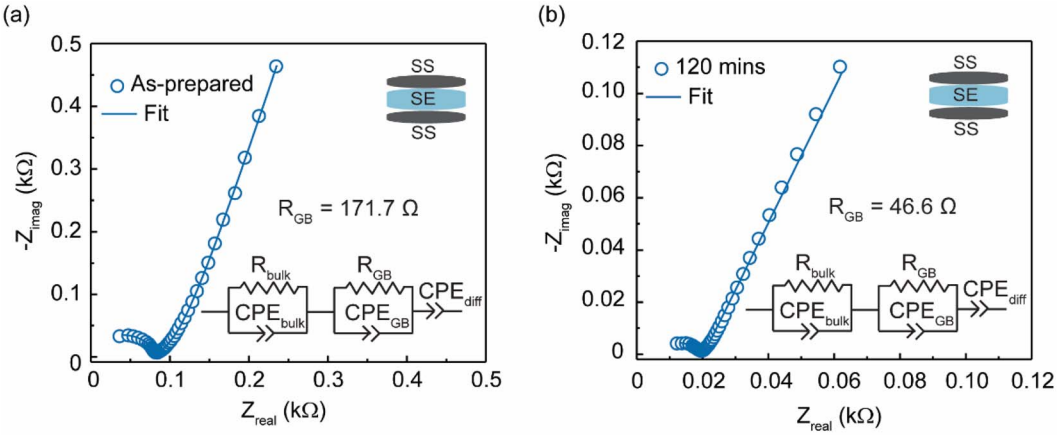

Fig. 8 Nyquist plots and equivalent circuit fitting of (a) as-prepared $Li_{3.6}In_7S_{11.8}Cl$ and (b) moisture-exposed $Li_{3.6}In_7S_{11.8}Cl$.

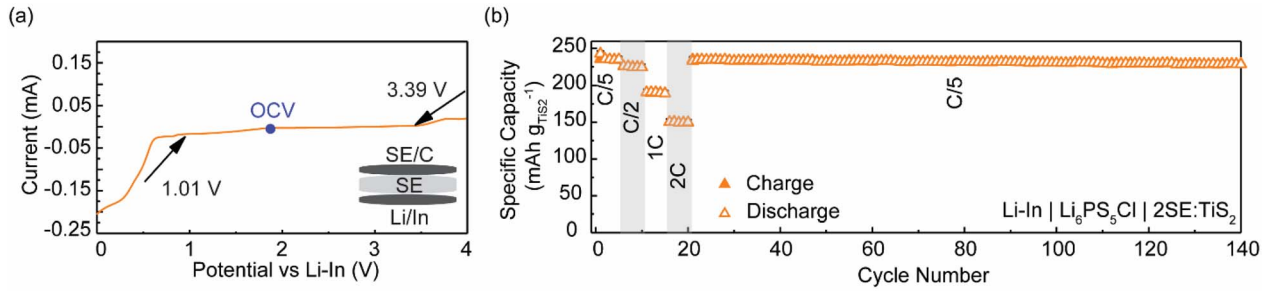

Fig. 9 (a) Linear sweep voltammetry (current–voltage) plot of $Li_{3.6}In_7S_{11.8}Cl$ (b) the rate performance and long-term cycling stability of a Li–In|Li_6PS_5Cl|2SE:TiS_2 cell (SE = $Li_{3.6}In_7S_{11.8}Cl$). C = 239 mA h g^{-1}.

revealed a significant reduction in grain boundary resistance (R_{GB}) from 171.7 Ω in the as-prepared sample to 46.6 Ω in the moisture-exposed sample. This confirms that the adsorbed water effectively facilitates Li^+ transport along/across grain boundaries. Since grain boundary resistance is often the limiting factor in polycrystalline solid electrolytes, the decrease in grain boundary resistance results in significantly enhanced Li^+ transport across/along the grain boundaries and the overall ionic conductivity.

Electrochemical stability and galvanostatic cycling of $Li_{3.6}In_7S_{11.8}Cl$

Linear sweep voltammetry (LSV) was utilized to assess the electrochemical stability window of $Li_{3.6}In_7S_{11.8}Cl$ at 25 °C. The electrochemical stability window signifies the voltage range within which the electrolytes and their components remain electrochemically inert.[35] Carbon, utilized as an electronic conductive medium offers a high surface area, facilitating sensitive detection of electric current generated from redox reactions.[35,36] Fig. 9a shows the linear sweep voltammogram of $Li_{3.6}In_7S_{11.8}Cl$. The anodic peak at ≈0.6 V *versus* Li–In is assigned to the lithiation of the carbon. Chloride ions (Cl^-) may undergo oxidation ($2Cl^- \rightarrow Cl_{2(g)} + 2e^-$) at voltages exceeding 3.74 V *versus* Li–In, based on their standard electrode potential.[65] The anodic peak around ≈3.8 V *versus* Li–In is indicative of oxidation of Cl species to Cl_2.[65–67] Therefore, the experimentally determined lower and upper electrochemical stability limit for $Li_{3.6}In_7S_{11.8}Cl$ is *ca.* 1.01–3.39 V *versus* Li–In.

Galvanostatic cycling at 22 °C was performed to evaluate the half-cell performance across various C-rates, with five cycles per rate, followed by 120 cycles at 0.2C, where C = 239 mA h g^{-1} (Fig. 9b). A Li–In|Li_6PS_5Cl|2($Li_{3.6}In_7S_{11.8}Cl$):TiS_2 half-cell was fabricated with TiS_2 as the cathode active material (CAM). Li–In anode was utilized due to its stability with solid electrolytes and reduced risk of micropore-induced short-circuiting.[2,35] The Li–In|Li_6PS_5Cl|2($Li_{3.6}In_7S_{11.8}Cl$):TiS_2 half-cell delivered an initial discharge capacity of *ca.* 240 mA h g^{-1}, eventually stabilizing at *ca.* 235 mA h g^{-1}. In the second cycle, the cell sustained a high discharge capacity of 226 mA h g^{-1} and maintained a consistent charge capacity of 225 mA h g^{-1}. Notably, at a high rate of 2C, the cell exhibited a robust performance, delivering a discharge capacity of 150 mA h g^{-1}. Upon reverting to 0.2C after 20 cycles, the Li–In|Li_6PS_5Cl|2($Li_{3.6}In_7S_{11.8}Cl$):TiS_2 half-cell demonstrated excellent long-term cycling stability, retaining *ca.* 96.8% of its capacity, over an extended period of 120 cycles.

Conclusion

In this study, an air- and moisture-stable solid electrolyte, $Li_{3.6}In_7S_{11.8}Cl$ (space group $Fd\bar{3}m$), is synthesized, delivering

a room-temperature ionic conductivity of 1.1 mS cm^{-1} with an activation energy of 0.26 eV. Structural characterization reveals a face-centered cubic arrangement of S^{2-}/Cl^{-}, stabilized by interstitial cations in a disordered anion sublattice. Notably, a 3D framework formed by tetrahedra Li_{8a} face-sharing with octahedra Li_{16c} promotes fast Li^{+} ion diffusion, supported by AIMD simulations. ^{6,7}Li NMR and relaxometry reveal fast ion dynamics of octahedral (16c) and tetrahedral (8a) Li^{+} sites, responsible for ion transport. $Li_{3.6}In_7S_{11.8}Cl$ exhibits stability against air and moisture and shows enhanced ionic conductivity to 4.2 mS cm^{-1} upon exposure, likely due to ion transport facilitated by the adsorbed water at grain boundaries. The water can be reversely removed upon heating to 350 °C without compromising the structural integrity. The stability is attributed to the structural stabilization provided by the strong covalent bonding between In^{3+} and S^{2-}.

Data availability

The data supporting this article have been included as part of the ESI.†

Author contributions

Ifeoluwa P. Oyekunle: data curation: lead; formal analysis: lead; investigation: lead; methodology: lead; software: lead; validation: lead; visualization: lead; writing – original draft: lead. Erica Truong: data curation: supporting; formal analysis: supporting; investigation: supporting; methodology: supporting; validation: supporting; visualization: supporting; writing – original draft: supporting. Tej Prasad Poudel: data curation: supporting; formal analysis: supporting; investigation: supporting; methodology: supporting; validation: supporting; visualization: supporting; writing – original draft: supporting. Yudan Chen: data curation: supporting; formal analysis: supporting; investigation: supporting; methodology: supporting; methodology: supporting; software: supporting; writing – original draft: supporting. Yongkang Jin: data curation: supporting investigation: supporting; validation: supporting; visualization: supporting; writing – original draft: supporting. Islamiyat A. Ojelade: data curation: supporting investigation: supporting; validation: supporting; visualization: supporting; writing – original draft: supporting. Michael J. Deck: data curation: supporting investigation: supporting; validation: supporting; writing – original draft: supporting. Bright Ogbolu: investigation: supporting; validation: supporting; visualization: supporting; writing – review & editing: supporting Md Mahinur Islam: data curation: supporting; validation: supporting; writing – review & editing: supporting Pawan K. Ojha: data curation: supporting; validation: supporting; writing – review & editing: supporting J. S. Raaj Vellore Winfred: data curation: supporting; formal analysis: supporting Dewen Hou: data curation: supporting. Hui Xiong: resources: supporting; supervision: supporting; validation: supporting. Chen Huang: data curation: supporting; software: supporting. Yan-Yan Hu, PhD: conceptualization: lead; formal analysis: lead; funding acquisition: lead; methodology: lead; project administration: lead; resources: lead; supervision: lead; validation: lead; visualization: equal; writing – original draft: equal; writing – review & editing: lead.

Conflicts of interest

The authors declare no conflict of interest.

Acknowledgements

The authors acknowledge support from the National Science Foundation under grant no. DMR-1847038. All solid-state NMR experiments were performed at the National High Magnetic Field Laboratory, which is supported by National Science Foundation Cooperative Agreement No. DMR-1644779 and DMR-2128556*. Hou and Xiong thank the support from the U.S. Department of Energy, Office of Science, Office of Basic Energy Sciences program under award number DE-SC0019121. Use of the Center for Nanoscale Materials and Advanced Photon Source, both DOE Office of Science user facility, was supported by the U.S. Department of Energy, Office of Science, Office of Basic Energy Sciences, under contract no. DE-AC02-06CH11357.

References

1 T. P. Poudel, E. Truong, I. P. Oyekunle, M. J. Deck, B. Ogbolu, Y. Chen, P. K. Ojha, T. N. D. D. Gamaralalage, S. V. Patel, Y. Jin, D. Hou, C. Huang, T. Li, Y. Liu, H. Xiong and Y.-Y. Hu, Sliceable, Moldable, and Highly Conductive Electrolytes for All-Solid-State Batteries, *ACS Energy Lett.*, 2024, **10**(1), 40–47.

2 T. P. Poudel, I. P. Oyekunle, M. J. Deck, Y. Chen, D. Hou, P. K. Ojha, B. O. Ogbolu, C. Huang, H. Xiong and Y. Y. Hu, Li(1.6)AlCl(3.4)S(0.6): a low-cost and high-performance solid electrolyte for solid-state batteries, *Chem. Sci.*, 2025, **16**, 2391.

3 H. Yamaguchi, A. Yao, S. Hiroi, H. Yamada, J.-c. Tseng, S. Shimono, F. Utsuno and K. Ohara, Formation process of halogen-rich argyrodite: elemental disordering of atomic arrangement at the 4a and 4d sites in a heat treatment, *J. Solid State Electrochem.*, 2024, **28**, 4419–4426.

4 S. Cho, Y. Kim, Y. Song, J. Ryu, K. Choi, J. Yang, S. H. Lee, S. G. Im and S. Park, Functional Polymer Thin Films for Establishing an Effective Electrode Interface in Sulfide-Based Solid-State Batteries, *Adv. Funct. Mater.*, 2024, **34**(32), 2314710.

5 K. H. Kim, M. J. Lee, M. Ryu, T. K. Liu, J. H. Lee, C. Jung, J. S. Kim and J. H. Park, Near-strain-free anode architecture enabled by interfacial diffusion creep for initial-anode-free quasi-solid-state batteries, *Nat. Commun.*, 2024, **15**(1), 3586.

6 K. G. Naik, D. Chatterjee and P. P. Mukherjee, Solid Electrolyte-Cathode Interface Dictates Reaction Heterogeneity and Anode Stability, *ACS Appl. Mater. Interfaces*, 2022, **14**(40), 45308–45319.

7 T. Kim, H. Chang, G. Song, S. Lee, K. Kim, S. Lee, J. Moon and K. T. Lee, Critical Factors Contributing to the Thermal Runaway of Thiophosphate Solid Electrolytes for

All-Solid-State Batteries, *Adv. Funct. Mater.*, 2024, **34**(42), 2404806.

8 H. Liu, Y. Chen, P.-H. Chien, G. Amouzandeh, D. Hou, E. Truong, I. P. Oyekunle, J. Bhagu, S. W. Holder, H. Xiong, P. Gor'kov, J. T. Rosenberg, S. C. Grant and Y.-Y. Hu, Dendrite formation in solid-state batteries arising from lithium plating and electrolyte reduction, *Nat. Mater.*, 2025, **24**, 581–588.

9 C. Wang, K. Adair and X. Sun, All-Solid-State Lithium Metal Batteries with Sulfide Electrolytes: Understanding Interfacial Ion and Electron Transport, *Acc. Mater. Res.*, 2021, **3**(1), 21–32.

10 H. Su, J. Li, Y. Zhong, Y. Liu, X. Gao, J. Kuang, M. Wang, C. Lin, X. Wang and J. Tu, A scalable Li-Al-Cl stratified structure for stable all-solid-state lithium metal batteries, *Nat. Commun.*, 2024, **15**(1), 4202.

11 P. Wang, H. Liu, S. Patel, J. E. Roberts, Y. Chen, B. Ogbolu, B. E. Francisco and Y. Y. Hu, Dual Polyanion Mechanism for Superionic Transport in BH4-Based Argyrodites, *Adv. Energy Mater.*, 2024, **14**(45), 2401549.

12 S. Chen, D. Xie, G. Liu, J. P. Mwizerwa, Q. Zhang, Y. Zhao, X. Xu and X. Yao, Sulfide solid electrolytes for all-solid-state lithium batteries: Structure, conductivity, stability and application, *Energy Storage Mater.*, 2018, **14**, 58–74.

13 A. Hayashi, N. Masuzawa, S. Yubuchi, F. Tsuji, C. Hotehama, A. Sakuda and M. Tatsumisago, A sodium-ion sulfide solid electrolyte with unprecedented conductivity at room temperature, *Nat. Commun.*, 2019, **10**(1), 5266.

14 R. Rajagopal, Y. Subramanian, S. Kang, J. Park and K.-S. Ryu, Improved interfacial stability of all-solid-state batteries using cation-anion co-doped glass electrolytes, *Commun. Mater.*, 2024, **5**(78), 1–13.

15 I. Hanghofer, M. Brinek, S. L. Eisbacher, B. Bitschnau, M. Volck, V. Hennige, I. Hanzu, D. Rettenwander and H. M. R. Wilkening, Substitutional disorder: structure and ion dynamics of the argyrodites Li(6)PS(5)Cl, Li(6)PS(5)Br and Li(6)PS(5)I, *Phys. Chem. Chem. Phys.*, 2019, **21**(16), 8489–8507.

16 W. Li, J. Liang, M. Li, K. R. Adair, X. Li, Y. Hu, Q. Xiao, R. Feng, R. Li, L. Zhang, S. Lu, H. Huang, S. Zhao, T.-K. Sham and X. Sun, Unraveling the Origin of Moisture Stability of Halide Solid-State Electrolytes by In Situ and Operando Synchrotron X-ray Analytical Techniques, *Chem. Mater.*, 2020, **32**(16), 7019–7027.

17 W. D. Jung, M. Jeon, S. S. Shin, J. S. Kim, H. G. Jung, B. K. Kim, J. H. Lee, Y. C. Chung and H. Kim, Functionalized Sulfide Solid Electrolyte with Air-Stable and Chemical-Resistant Oxysulfide Nanolayer for All-Solid-State Batteries, *ACS Omega*, 2020, **5**(40), 26015–26022.

18 X. Lu, O. Camara, Z. Liu, A. Windmüller, C. L. Tsai, H. Tempel, S. Yu, H. Kungl and R. A. Eichel, Tuning the moisture stability of multiphase β-Li3PS4 solid electrolyte materials, *Electrochem. Sci. Adv.*, 2022, **3**(2), e2100208.

19 G. Kresse and J. Furthmuller, Efficient iterative schemes for ab initio total-energy calculations using a plane-wave basis set, *Phys. Rev. B: Condens. Matter Mater. Phys.*, 1996, **54**(16), 11169.

20 P. E. Blochl, Projector augmented-wave method, *Phys. Rev. B Condens. Matter*, 1994, **50**(24), 17953–17979.

21 J. P. Perdew, K. Burke and M. Ernzerhof, Generalized Gradient Approximation Made Simple, *Phys. Rev. Lett.*, 1996, **77**(18), 3865–3868.

22 S. P. Ong, W. D. Richards, A. Jain, G. Hautier, M. Kocher, S. Cholia, D. Gunter, V. L. Chevrier, K. A. Persson and G. Ceder, Python Materials Genomics (pymatgen): A robust, open-source python library for materials analysis, *Comput. Mater. Sci.*, 2013, **68**, 314–319.

23 A. Y. Toukmaji and J. A. Board Jr, Ewald summation techniques in perspective: a survey, *Comput. Phys. Commun.*, 1996, **95**, 73–92.

24 S. J. Clark, I. Matthew, D. Segall, C. J. Pickard, P. J. Hasnip, M. I. J. Probert, K. Refson and M. C. PayneII, First Principles Methods using CASTEP, *Z. Kristallogr. Cryst. Mater.*, 2005, **220**, 567–570.

25 M. D. Segall, P. J. D. Lindan, M. J. Probert, C. J. Pickard, P. J. Hasnip, S. J. Clark and M. C. Payne, First-principles simulation: ideas, illustrations and the CASTEP code, *J. Phys.: Condens. Matter*, 2002, **14**, 2717–2744.

26 D. C. Liu and J. Nocedal, On the Limited Memory BFGS Method for Large Scale Optimization, *Math. Program.*, 1989, **45**, 503–528.

27 J. Nocedal, Updating Quasi-Newton Matrices With Limited Storage, *Math. Comput.*, 1980, **35**(151), 773–782.

28 L. L. Wong, K. C. Phuah, R. Dai, H. Chen, W. S. Chew and S. Adams, Bond Valence Pathway Analyzer—An Automatic Rapid Screening Tool for Fast Ion Conductors within softBV, *Chem. Mater.*, 2021, **33**(2), 625–641.

29 S. Adams, From bond valence maps to energy landscapes for mobile ions in ion-conducting solids, *Solid State Ionics*, 2006, **177**(19–25), 1625–1630.

30 S. V. Patel, S. Banerjee, H. Liu, P. Wang, P.-H. Chien, X. Feng, J. Liu, S. P. Ong and Y.-Y. Hu, Tunable Lithium-Ion Transport in Mixed-Halide Argyrodites Li6–xPS5–xClBrx: An Unusual Compositional Space, *Chem. Mater.*, 2021, **33**(4), 1435–1443.

31 C. Adenis, J. Olivier-Fourcade, J.-C. Jumas and E. Philippot, Etude structurale par spectroscopie Mössbauer et rayons X de spinelles lacunaires de type In2S3, *Rev. Chim. Miner.*, 1987, **24**(1), 10–21.

32 L. Zhou, C. Y. Kwok, A. Shyamsunder, Q. Zhang, X. Wu and L. F. Nazar, A new halospinel superionic conductor for high-voltage all solid state lithium batteries, *Energy Environ. Sci.*, 2020, **13**(7), 2056–2063.

33 V. Tsurkan, H.-A. Krug von Nidda, J. Deisenhofer, P. Lunkenheimer and A. Loidl, On the complexity of spinels: Magnetic, electronic, and polar ground states, *Phys. Rep.*, 2021, **926**, 1–86.

34 N. Bloembergen, E. M. Purcell and R. V. Pound, Relaxation Effects in Nuclear Magnetic Resonance Absorption, *Phys. Rev.*, 1948, **73**(7), 679–712.

35 T. P. Poudel, M. J. Deck, P. Wang and Y. Y. Hu, Transforming Li3PS4 Via Halide Incorporation: a Path to Improved Ionic Conductivity and Stability in All-Solid-State Batteries, *Adv. Funct. Mater.*, 2023, **34**(4), 2309656.

36 M. J. Deck, P. H. Chien, T. P. Poudel, Y. Jin, H. Liu and Y. Y. Hu, Oxygen-Induced Structural Disruption for Improved Li+ Transport and Electrochemical Stability of Li3PS4, *Adv. Energy Mater.*, 2023, **14**(4), 2302785.

37 K. Kaup, K. Bishop, A. Assoud, J. Liu and L. F. Nazar, Fast Ion-Conducting Thioboracite with a Perovskite Topology and Argyrodite-like Lithium Substructure, *J. Am. Chem. Soc.*, 2021, **143**(18), 6952–6961.

38 Y. Zhu and Y. Mo, Materials Design Principles for Air-Stable Lithium/Sodium Solid Electrolytes, *Angew Chem. Int. Ed. Engl.*, 2020, **59**(40), 17472–17476.

39 J. Sang, K. Pan, B. Tang, Z. Zhang, Y. Liu and Z. Zhou, One Stone, Three Birds: An Air and Interface Stable Argyrodite Solid Electrolyte with Multifunctional Nanoshells, *Adv. Sci.*, 2023, **10**(32), e2304117.

40 Y.-T. Chen, M. A. T. Marple, D. H. S. Tan, S.-Y. Ham, B. Sayahpour, W.-K. Li, H. Yang, J. B. Lee, H. J. Hah, E. A. Wu, J.-M. Doux, J. Jang, P. Ridley, A. Cronk, G. Deysher, Z. Chen and Y. S. Meng, Investigating dry room compatibility of sulfide solid-state electrolytes for scalable manufacturing, *J. Mater. Chem. A*, 2022, **10**(13), 7155–7164.

41 M. Yang, L. Chen, H. Li and F. Wu, Air/Water Stability Problems and Solutions for Lithium Batteries, *Adv. Energy Mater.*, 2022, **2022**, 1–41.

42 Y. Morino, H. Sano, T. Takahashi, N. Miyashita, A. Sakuda and A. Hayashi, Hydrogen Components of a Sulfide-based Argyrodite-Type Solid Electrolyte after Moisture Exposure, *J. Phys. Chem. C*, 2023, **127**(28), 13616–13622.

43 T. A. Yersak, Y. Zhang, F. Hao and M. Cai, Moisture Stability of Sulfide Solid-State Electrolytes, *Front. Energy Res.*, 2022, **10**, 1–9.

44 Y. Wang, X. Lu, C. Zheng, X. Liu, Z. Chen, W. Yang, J. Lin and F. Huang, Chemistry Design Towards a Stable Sulfide-Based Superionic Conductor Li(4) Cu(8) Ge(3) S(12), *Angew Chem. Int. Ed. Engl.*, 2019, **58**(23), 7673–7677.

45 C. Wang, J. Hao, J. Wu, H. Shi, L. Fan, J. Wang, Z. Wang, Z. Wang, L. Yang, Y. Gao, X. Yan and Y. Gu, Enhanced Air Stability and Li Metal Compatibility of Li-Argyrodite Electrolytes Triggered by In2O3 Co-Doping for All-Solid-State Li Metal Batteries, *Adv. Funct. Mater.*, 2024, **34**(18), 2313308.

46 Y. Fu, Z. Gong, D. Li, Y. Liu, X. Zhou, Y. Yang and Q. Jiao, Zn doping for enhanced sodium-ion conductivity and air stability in Na3SbS4 solid electrolyte, *J. Mater. Sci.*, 2024, **59**(7), 3009–3017.

47 R. Guo, K. Zhang, W. Zhao, Z. Hu, S. Li, Y. Zhong, R. Yang, X. Wang, J. Wang, C. Wu and Y. Bai, Interfacial Challenges and Strategies toward Practical Sulfide-Based Solid-State Lithium Batteries, *Adv. Energy Mater.*, 2023, **4**(1), 1–31.

48 Z. Yu, S. L. Shang, J. H. Seo, D. Wang, X. Luo, Q. Huang, S. Chen, J. Lu, X. Li, Z. K. Liu and D. Wang, Exceptionally High Ionic Conductivity in Na(3) P(0.62) As(0.38) S(4) with Improved Moisture Stability for Solid-State Sodium-Ion Batteries, *Adv. Mater.*, 2017, **29**(16), 1605561.

49 J. Liang, X. Li, C. Wang, J. T. Kim, R. Yang, J. Wang and X. Sun, Current Status and Future Directions in Environmental Stability of Sulfide Solid-State Electrolytes for All-Solid-State Batteries, *Adv. Energy Mater.*, 2023, **4**, 1–14.

50 Y. E. Choi, K. H. Park, D. H. Kim, D. Y. Oh, H. R. Kwak, Y. G. Lee and Y. S. Jung, Coatable Li(4) SnS(4) Solid Electrolytes Prepared from Aqueous Solutions for All-Solid-State Lithium-Ion Batteries, *ChemSusChem*, 2017, **10**(12), 2605–2611.

51 A.-K. Hatz, I. Moudrakovski, S. Bette, M. W. Terban, M. Etter, M. Joos, N. M. Vargas-Barbosa, R. E. Dinnebier and B. V. Lotsch, Fast Water-Assisted Lithium Ion Conduction in Restacked Lithium Tin Sulfide Nanosheets, *Chem. Mater.*, 2021, **33**(18), 7337–7349.

52 M. Deluca, H. Hu, M. N. Popov, J. Spitaler and T. Dieing, Advantages and developments of Raman spectroscopy for electroceramics, *Commun. Mater.*, 2023, **4**(1), 78–92.

53 Y. Chen, P. Wang, E. Truong, B. Ogbolu, Y. Jin, I. Oyekunle, H. Liu, M. M. Islam, T. Poudel, C. Huang, I. Hung, Z. Gan and Y. Y. Hu, Superionic Conduction in K(3)SbS(4) Enabled by Cl-Modified Anion Lattice, *Angew Chem. Int. Ed. Engl.*, 2024, **63**(35), e202408574.

54 P. Pistor, J. M. Merino Alvarez, M. Leon, M. di Michiel, S. Schorr, R. Klenk and S. Lehmann, Structure reinvestigation of alpha-, beta- and gamma-In2S3, *Acta Crystallogr., Sect. B: Struct. Sci., Cryst. Eng. Mater.*, 2016, **72**(3), 410–415.

55 L. A. Wägele, D. Rata, G. Gurieva and R. Scheer, Structural analysis of co-evaporated In2S3 and In2S3:V for solar cell absorber applications, *Phys. Status Solidi C*, 2017, **14**(6), 1600204.

56 H. Izadneshana and V. F. Gremenok, Micro Structural Analysis of In2S3 Thin Films by Raman Spectroscopy, *J. Appl. Spectrosc.*, 2014, **81**(5), 765–770.

57 S. Gallego-Parra, O. Gomis, R. Vilaplana, V. P. Cuenca-Gotor, D. Martinez-Garcia, P. Rodriguez-Hernandez, A. Munoz, A. Romero, A. Majumdar, R. Ahuja, C. Popescu and F. J. Manjon, Pressure-induced order-disorder transitions in beta-In(2)S(3): an experimental and theoretical study of structural and vibrational properties, *Phys. Chem. Chem. Phys.*, 2021, **23**(41), 23625–23642.

58 A. I. Ali, M. Ibrahim and A. Hassen, New fabrication method for di-indium tri-sulfuric (In(2)S(3)) thin films, *Sci. Rep.*, 2022, **12**(1), 7033.

59 Y. Suffren, F.-G. Rollet and C. Reber, Raman Spectroscopy of Transition Metal Complexes: Molecular Vibrational Frequencies, Phase Transitions, Isomers, and Electronic Structure, *Comments Inorg. Chem.*, 2011, **32**(5–6), 246–276.

60 M. Joos, C. Schneider, A. Münchinger, I. Moudrakovski, R. Usiskin, J. Maier and B. V. Lotsch, Impact of hydration on ion transport in Li2Sn2S5·xH2O, *J. Mater. Chem. A*, 2021, **9**(30), 16532–16544.

61 F. Xu, S. Leclerc and D. Canet, NMR relaxometry study of the interaction of water with a Nafion membrane under acid, sodium, and potassium forms. Evidence of two types of bound water, *J. Phys. Chem. B*, 2013, **117**(21), 6534–6540.

62 G. A. H. Ludlam, S. J. P. Gnaniah, R. Degl'Innocenti, G. Gupta, A. J. Wain and H. Lin, Measurement of Water Uptake and States in Nafion Membranes Using Humidity-

Controlled Terahertz Time-Domain Spectroscopy, *ACS Sustain. Chem. Eng.*, 2024, **12**(20), 7924–7934.

63 H. Furusawa, R. Konishi, D. Mori, H. Horino, T. Horiba, Y. Takeda, J. Takada, O. Yamamoto and N. Imanishi, Biogenous iron oxide (L-BIOX) as a high capacity anode material for lithium ion batteries, *Electrochim. Acta*, 2018, **281**, 227–236.

64 Z. W. B. Iton, B. C. Lee, A. Y. Jiang, S. S. Kim, M. J. Brady, S. Shaker and K. A. See, Water Vapor Induced Superionic Conductivity in ZnPS(3), *J. Am. Chem. Soc.*, 2023, **145**(24), 13312–13325.

65 S. Ohno, C. Rosenbach, G. F. Dewald, J. Janek and W. G. Zeier, Linking Solid Electrolyte Degradation to Charge Carrier Transport in the Thiophosphate-Based Composite Cathode toward Solid-State Lithium-Sulfur Batteries, *Adv. Funct. Mater.*, 2021, **31**(18), 2010620.

66 H. Kwak, S. Wang, J. Park, Y. Liu, K. T. Kim, Y. Choi, Y. Mo and Y. S. Jung, Emerging Halide Superionic Conductors for All-Solid-State Batteries: Design, Synthesis, and Practical Applications, *ACS Energy Lett.*, 2022, **7**(5), 1776–1805.

67 Y.-T. Chen, D. H. S. Tan, S.-Y. Ham, B. Sayahpour, J. B. Lee, Y. Kim, M.-S. Song, L. H. B. Nguyen, J. A. S. Oh, P. Ridley, A. Cronk, G. Deysher, J. Jang, Z. Chen and Y. S. Meng, Investigating Dry Room Compatibility of Chloride Solid-State Electrolytes for Scalable Manufacturing, *J. Electrochem. Soc.*, 2023, **170**(8), 080521.